The Astrophysical Journal, 999:100 (12pp), 2026 March 1 https://doi.org/10.3847/1538-4357/ae4023
© 2026. The Author(s). Published by the American Astronomical Society.
OPEN ACCESS

Orbital Classification in Rotating Bar Potentials Using an Empirical Proxy of the Second Integral of Motion

Tian-Ye Xia[1], Juntai Shen[1,2,3], John Magorrian[4], and Yu-jing Qin[5]
[1] Department of Astronomy, School of Physics and Astronomy, Shanghai Jiao Tong University, 800 Dongchuan Road, Shanghai 200240, People's Republic of China; jtshen@sjtu.edu.cn
[2] State Key Laboratory of Dark Matter Physics, School of Physics and Astronomy, Shanghai Jiao Tong University, Shanghai 200240, People's Republic of China
[3] Key Laboratory for Particle Astrophysics and Cosmology (MOE)/Shanghai Key Laboratory for Particle Physics and Cosmology, Shanghai 200240, People's Republic of China
[4] Rudolf Peierls Centre for Theoretical Physics, Beecroft Building, Parks Road, Oxford, OX1 3PU, UK; john.magorrian@physics.ox.ac.uk
[5] Department of Astronomy and Astrophysics, Cahill Center for Astrophysics, California Institute of Technology, MC 249-17, 1200 East California Boulevard, Pasadena, CA 91125, USA
Received 2025 December 30; revised 2026 January 30; accepted 2026 January 30; published 2026 February 26

Abstract

We present a novel method for classifying two-dimensional orbits in rotating bar potentials based on an empirical proxy for the second integral of motion, calibrated angular momentum (CAM), which is defined as the ratio of the time-averaged angular momentum ($\overline{L_z}$) to its temporal dispersion (σ_{L_z}) in the corotating frame. We show that CAM is determined by the ratio of the azimuthal to radial actions (J_ϕ'/J_r') in the analytical Freeman bar model. We then construct a new parameter space defined by CAM versus the rms radius ($R_{\rm rms}$) and apply this framework to orbits in several representative rotating bar potentials. In the CAM–$R_{\rm rms}$ plane, periodic orbits generate well-defined branches separating distinct regions corresponding to different orbital families. Several of these branches enclose isolated areas that can be associated with specific orbital families, such as the x_2 orbital family. We further validate the method using orbits from test-particle simulations, which show a well-ordered and nonoverlapping distribution of orbital families in the CAM–$R_{\rm rms}$ plane. Since CAM is fundamentally linked to intrinsic orbital properties and readily applied to three-dimensional orbits in N-body simulations, our results establish the CAM–$R_{\rm rms}$ plane as a robust and efficient framework for orbit classification in rotating bars that complements conventional methods.

Unified Astronomy Thesaurus concepts: Orbits (1184); Barred spiral galaxies (136); Galaxy dynamics (591)

1. Introduction

Stellar orbits constitute the fundamental building blocks of galactic dynamics. Numerous studies have explored the structure and evolution of orbital families in rotating bar potentials, as barred spiral galaxies account for nearly two-thirds of all spiral galaxies, including our Milky Way (J. Binney et al. 1991; J. Shen et al. 2010; J. Shen & X.-W. Zheng 2020).

In the two-dimensional (2D) case, the most important orbital families include the prograde x_1 orbits elongated along the major bar axis, the retrograde x_4 orbits oriented perpendicular to the bar, and the prograde x_2 (stable) and x_3 (unstable) orbits, which are also perpendicular to the bar (G. Contopoulos & P. Grosbol 1989; J. A. Sellwood & A. Wilkinson 1993; J. Binney & S. Tremaine 2008). The x_1 family dominates the orbital population in self-gravitating bars, providing the primary support for the bar structure. In contrast, x_4 orbits are typically rounder in shape and are predominantly found at smaller radii (L. S. Sparke & J. A. Sellwood 1987; G. Contopoulos & P. Grosbol 1989). x_2 and x_3 orbits exist only when an inner Lindblad resonance exists. They could vanish in systems with low central density, rapid bar rotation, or particularly strong bars (G. D. van Albada 1983; L. S. Sparke & J. A. Sellwood 1987; J. A. Sellwood & A. Wilkinson 1993; M. Valluri et al. 2016).

In three-dimensional (3D) models, the overall picture of orbital families remains broadly consistent, especially for periodic orbits. The dominant contribution still arises from vertical bifurcations of the x_1 family, which extend the 2D orbital backbone into the vertical dimension. Several studies have demonstrated that 3D bars are composed primarily of these vertically extended x_1 descendants, supplemented by a few additional orbital families (D. Pfenniger & D. Friedli 1991; J. A. Sellwood & A. Wilkinson 1993; C. Skokos et al. 2002a, 2002b).

Conventional methods for orbital classification include the Poincaré surface of section (SoS), which projects orbital trajectories onto a 2D phase-space plane. In this representation, different orbital families exhibit distinct patterns: periodic orbits appear as discrete points, regular orbits stay on invariant curves, chaotic orbits populate a diffuse "sea," and higher-order resonant orbits occupy small island-like structures between the regular and chaotic regions. Orbital families often form bull's-eye patterns around parent orbits, enabling a qualitative classification of the orbital structure (H. Poincaré 1892; J. A. Sellwood & A. Wilkinson 1993; J. Shen & J. A. Sellwood 2004; J. Binney & S. Tremaine 2008).

However, despite its widespread recognition, the SoS method suffers from notable limitations. First, it is inherently energy-dependent and applicable only to orbits at a fixed energy, making it less suitable for analyzing orbits with a continuous energy distribution, as are often encountered in N-body simulations. Second, it does not scale well to higher dimensions: in the 3D systems, extracting a meaningful 2D section from five-dimensional energy-constrained phase space becomes challenging and risks obscuring key dynamical features (D. D. Carpintero & L. A. Aguilar 1998).

Another well-established diagnostic tool often used to aid orbital classification is frequency analysis, which can be

Original content from this work may be used under the terms of the Creative Commons Attribution 4.0 licence. Any further distribution of this work must maintain attribution to the author(s) and the title of the work, journal citation and DOI.

applied to both 2D and 3D orbits (J. Binney & D. Spergel 1982; J. Laskar 1993; D. D. Carpintero & L. A. Aguilar 1998; N. Voglis et al. 2007; M. Valluri et al. 2010, 2016). This technique constructs frequency maps by performing a spectral decomposition of orbits, where distinct orbital families appear as clusters of points centered around their resonant parent orbits. These resonances manifest as thin lines in the frequency space (M. Valluri et al. 2016). Despite its utility, frequency analysis suffers from several limitations. First, the identification of fundamental frequencies can be technically challenging and computationally expensive. Second, frequency maps depend on the choice of coordinate system, which can cause resonant orbits to mix with others when different coordinates are used (N. Voglis et al. 2007; M. Valluri et al. 2016). Moreover, degeneracies can arise because different orbital families may share the same resonance. For example, the x_2 and x_4 orbits can both be associated with the 2:1 radial-to-azimuthal resonance, making them difficult to distinguish based solely on their spectral signatures.

To overcome these issues, we adopt an alternative classification framework based on an empirical proxy for the second integral of motion, originally introduced by Y.-J. Qin & J. Shen (2021, hereafter QS21). The second integral of motion (I_2) is a conserved quantity that constrains the phase space of regular orbits to a lower dimension. Unlike the Hamiltonian (i.e., the constant Jacobi energy, which combines the energy and angular momentum in the inertial frame through the relation $E_J = E - \boldsymbol{\Omega}_b \cdot \boldsymbol{L}$ in rotating bar potentials), I_2 typically lacks analytic expressions and is referred to as a nonclassical integral of motion. Although these integrals can sometimes be inferred from the SoS, they remain difficult to isolate or define in general bar potentials (J. Binney & S. Tremaine 2008). To address this challenge, QS21 proposed an empirical proxy for I_2 in rotating bar potentials named the calibrated angular momentum (CAM). This quantity is defined as the ratio of the time-averaged angular momentum ($\overline{L_z}$) to its temporal dispersion (σ_{L_z}) in the corotating frame. Their analysis revealed that the often-ignored physical quantity σ_{L_z} actually contains valuable information, and that orbits with a constant Jacobi energy form a tight sequence in the $\overline{L_z}$–σ_{L_z} plane. This sequence traces the main orbital families in the Poincaré SoS from the x_4 to x_1 orbits and is accompanied by a monotonic variation in CAM, thereby demonstrating the effectiveness of CAM as an empirical proxy for I_2.

The CAM framework offers several key advantages over traditional classification methods. First, it is effectively Hamiltonian-independent. By incorporating the Jacobi energy or other E_J-related quantities as an additional parameter in the classification space, CAM can accommodate orbits spanning a broad range of Jacobi energies, making it inherently more suitable for analyzing realistic bar models than the SoS method, which is limited to iso-E_J slices. Moreover, in contrast to frequency-based techniques, CAM exhibits greater robustness against degeneracies among orbital families, as it does not rely on resonance structures that may overlap across different orbit types. Third, the CAM framework is naturally extensible to 3D orbits. By incorporating an additional proxy for the third integral of motion, the method can potentially describe 3D orbits using just three parameters, which may provide a more visually intuitive alternative to SoS-based approaches.

Our main motivation is to investigate the effectiveness of CAM for 2D orbital classification in rotating bar potentials. While QS21 focused primarily on the empirical and numerical properties of CAM, we begin by investigating its analytical implications within the Freeman bar model, aiming to gain insight into the physical meaning of this proxy. Next, we evaluate the performance of CAM for orbital classification across three representative rotating bar potentials: the Freeman bar, the logarithmic bar, and the Ferrers bar. In addition to the $\overline{L_z}$–σ_{L_z} plane studied by QS21, we introduce a new parameter plane defined by CAM and the rms radius ($R_{\rm rms} = \sqrt{\overline{R^2}}$),[6] where the average is taken over time along the orbit using a uniform time interval. We first explore the behavior of iso-E_J and periodic orbits within the CAM framework, finding that periodic orbits form well-defined branches in the CAM–$R_{\rm rms}$ plane that effectively partition the space into domains corresponding to specific orbital families. We then extend the analysis to test-particle orbits rather than orbits constrained by fixed Jacobi energies, thereby demonstrating the applicability of this method to realistic N-body simulations. Our analyses show that different orbital families exhibit a well-ordered distribution in the CAM–$R_{\rm rms}$ plane. These results highlight CAM as a robust and efficient tool for orbital classification.

The paper is organized as follows. In Section 2, we review the definition of CAM and examine its implications within the analytical Freeman bar model. Section 3 introduces the CAM–$R_{\rm rms}$ plane and explores the behavior of iso-E_J and periodic orbits in this framework. In Section 4, we extend the analysis to test-particle orbits. We discuss the broader implications of our results in Section 5 and summarize in Section 6.

2. Physical Interpretation of CAM

CAM was first introduced by QS21 as a numerical proxy of I_2 in a 2D rotating logarithmic bar potential. It is defined as the ratio of the time-averaged angular momentum in the bar corotating frame to its temporal dispersion, expressed as

$$\mathrm{CAM} = \frac{\overline{L_z}}{\sigma_{L_z}}. \tag{1}$$

While CAM has been numerically demonstrated to serve as an empirical proxy for I_2, its physical nature remains to be understood. In this section, we investigate its physical meaning by expressing CAM as a function of the orbital actions in a simple analytical bar model. We focus on the actions $\boldsymbol{J}$ because they are integrals of motion that form a complete set of canonical coordinates with angle variables $\boldsymbol{\theta}$ (J. Binney & S. Tremaine 2008). Moreover, some specific potentials admit analytical expressions for these actions, including the Freeman bar model that we adopt in this section.

The Freeman bar (K. C. Freeman 1966; K. C. Freeman & L. Mestel 1966) represents one of the simplest analytical bar models, in which all orbits can be expressed analytically. It produces a quadratic potential:

$$\Phi(x, y) = \frac{1}{2}(\Omega_x^2 x^2 + \Omega_y^2 y^2). \tag{2}$$

Here we set $\Omega_x = 1$ and $\Omega_y = \sqrt{2}$. The potential is rotating with a fixed pattern speed of $\Omega_b = 0.5$.

[6] Throughout this paper, we use $R_{\rm rms}$ to characterize the orbital size, but we do confirm that the mean absolute radius ($\overline{|R|}$) produces comparable results.

The effective potential of the Freeman bar is

$$\Phi_{\rm eff} = \frac{1}{2}\Omega_x^2 x^2 + \frac{1}{2}\Omega_y^2 y^2 - \frac{1}{2}\Omega_{\rm b}{}^2(x^2+y^2) = \frac{1}{2}\Phi_{xx}x^2 + \frac{1}{2}\Phi_{yy}y^2, \quad (3)$$

where $\Phi_{xx} = \Omega_x^2 - \Omega_{\rm b}{}^2$ and $\Phi_{yy} = \Omega_y^2 - \Omega_{\rm b}{}^2$. Here, (x, y) are Cartesian coordinates in the corotating frame.

Solving the equation of motion $\ddot{\boldsymbol{x}} = -\boldsymbol{\nabla}\Phi_{\rm eff} - 2\boldsymbol{\Omega}_{\rm b} \times \dot{\boldsymbol{x}}$, the orbits of the Freeman bar model are (K. C. Freeman 1966)

$$x = X_\alpha \cos\theta_\alpha + X_\beta \cos\theta_\beta, \quad y = Y_\alpha \sin\theta_\alpha + Y_\beta \sin\theta_\beta, \quad (4)$$

where $\theta_\alpha = \alpha t + \phi_\alpha$ and $\theta_\beta = \beta t + \phi_\beta$, and where α and β are the two positive roots ($\alpha^2 < \Phi_{xx} < \Phi_{yy} < \beta^2$) of the equation

$$x^4 - x^2(\Phi_{xx} + \Phi_{yy} + 4\Omega_{\rm b}{}^2) + \Phi_{xx}\Phi_{yy} = 0. \quad (5)$$

A general orbit in a Freeman bar is the superposition of two ellipses: the prograde α-ellipse along the bar axis with frequency α (or x_1 orbits) and the retrograde β-ellipse perpendicular to the bar axis with frequency β (or x_4 orbits). There are no x_2 or x_3 orbital families in the Freeman bar.

The axial ratios q_α and q_β of the α-ellipse and the β-ellipse are two constants, as below,[7]

$$q_\alpha = \frac{Y_\alpha}{X_\alpha} = \frac{\Phi_{xx} - \alpha^2}{2\Omega_b \alpha} = \frac{2\Omega_b \alpha}{\Phi_{yy} - \alpha^2}, \quad q_\beta = \frac{Y_\beta}{X_\beta} = \frac{\Phi_{xx} - \beta^2}{2\Omega_b \beta} = \frac{2\Omega_b \beta}{\Phi_{yy} - \beta^2}, \quad (6)$$

where $q_\alpha > 0$ and $q_\beta < 0$, indicating prograde motion for the α-ellipse and retrograde motion for the β-ellipse, respectively.

The angular momentum in the corotating frame is $L_z = x\dot{y} - y\dot{x}$, which can be rewritten as

$$L_z = \alpha X_\alpha Y_\alpha + \beta X_\beta Y_\beta + (\alpha q_\alpha + \beta q_\beta) X_\alpha X_\beta \cos\theta_\alpha \cos\theta_\beta + (\alpha q_\beta + \beta q_\alpha) X_\alpha X_\beta \sin\theta_\alpha \sin\theta_\beta. \quad (7)$$

For nonzero $\Omega_{\rm b}$, the second and third terms cannot vanish simultaneously as $\alpha \neq \beta$, except in the case of periodic orbits for which $X_\alpha = 0$ or $X_\beta = 0$.

Thus, the time-averaged L_z is

$$\overline{L_z} = \alpha q_\alpha X_\alpha{}^2 + \beta q_\beta X_\beta^2. \quad (8)$$

The dispersion of L_z can be obtained as

$$\sigma_{L_z} = \left[\frac{1}{8}(\alpha+\beta)^2(q_\alpha+q_\beta)^2 + \frac{1}{8}(\alpha-\beta)^2(q_\alpha-q_\beta)^2\right]^{\frac{1}{2}} X_\alpha X_\beta. \quad (9)$$

Therefore, the relationship between $\overline{L_z}$ and σ_{L_z} can be expressed as

$$\frac{\overline{L_z}^2}{A^2} + \frac{\sigma_{L_z}{}^2}{B^2} = 1, \quad (10)$$

where A and B are constants that depend only on α, β, q_α, and q_β.

Orbits under a fixed $E_{\rm J}$ satisfy

$$E_{\rm J} = \frac{1}{2}X_\alpha{}^2(\alpha^2 + \Phi_{yy}q_\alpha{}^2) + \frac{1}{2}X_\beta{}^2(\beta^2 + \Phi_{yy}q_\beta{}^2). \quad (11)$$

Thus, the $\overline{L_z}$–σ_{L_z} distribution for orbits in a given Freeman bar potential at fixed $E_{\rm J}$ lies along the upper half of an ellipse, as shown by the black curves in the left panel of Figure 1. Along this half-ellipse curve, from the bottom left to the bottom right, a clear transition from x_4 to x_1 orbits emerges, confirming that CAM traces the variations of I_2, as suggested in QS21. We also plot the CAM contours in the blue dashed curves of the left panel of Figure 1, which appear as straight rays emanating from the origin.

Since this potential corresponds to a 2D harmonic oscillator, the action-angle variables can be written simply as (K. C. Freeman 1966)

$$J_\alpha = \frac{1}{2}(\alpha q_\alpha - \beta q_\beta) q_\alpha X_\alpha^2, \quad J_\beta = -\frac{1}{2}(\alpha q_\alpha - \beta q_\beta) q_\beta X_\beta^2, \quad \theta_\alpha = \alpha t + \phi_\alpha, \quad \theta_\beta = \beta t + \phi_\beta. \quad (12)$$

The actions J_α and J_β are proportional to X_α^2 and X_β^2, respectively, which in turn scale with the areas enclosed by the α- and β-ellipses in a given potential, thereby quantifying the extent of motion along each ellipse.

The Hamiltonian can be written as

$$H = \alpha J_\alpha + \beta J_\beta \equiv E_{\rm J}. \quad (13)$$

CAM can then be expressed as a function of J_α and J_β,

$$\mathrm{CAM} = \frac{\overline{L_z}}{\sigma_{L_z}} = C_1 \frac{\alpha J_\alpha - \beta J_\beta}{\sqrt{J_\alpha J_\beta}}, \quad (14)$$

where C_1 is a constant.

While J_α and J_β are actions defined specifically for the harmonic oscillator, we next seek an alternative set of actions associated with the radial and azimuthal motions, which can provide information applicable to more general potentials. We therefore introduce a new set of action-angle variables $(J_r', J_\phi', \theta_r', \theta_\phi')$, defined through the generating function $S(\theta_\alpha, \theta_\beta, J_r', J_\phi')$,

$$S(\theta_\alpha, \theta_\beta, J_r', J_\phi') = \theta_\alpha\left(J_r' + \frac{s+1}{2}J_\phi'\right) + \theta_\beta\left(J_r' + \frac{s-1}{2}J_\phi'\right), \quad (15)$$

where $s = \mathrm{sgn}(J_\phi')$. The new set of action-angle variables can then be written as

$$J_r' = \frac{1}{2}[J_\alpha + J_\beta - s(J_\alpha - J_\beta)], \quad J_\phi' = J_\alpha - J_\beta, \quad \theta_r' = \theta_\alpha + \theta_\beta, \quad \theta_\phi' = \frac{1}{2}[s(\theta_\alpha + \theta_\beta) + (\theta_\alpha - \theta_\beta)]. \quad (16)$$

[7] q_α and q_β correspond to k_α and k_β in K. C. Freeman (1966), while X_α and X_β correspond to A_α and A_β in that paper.

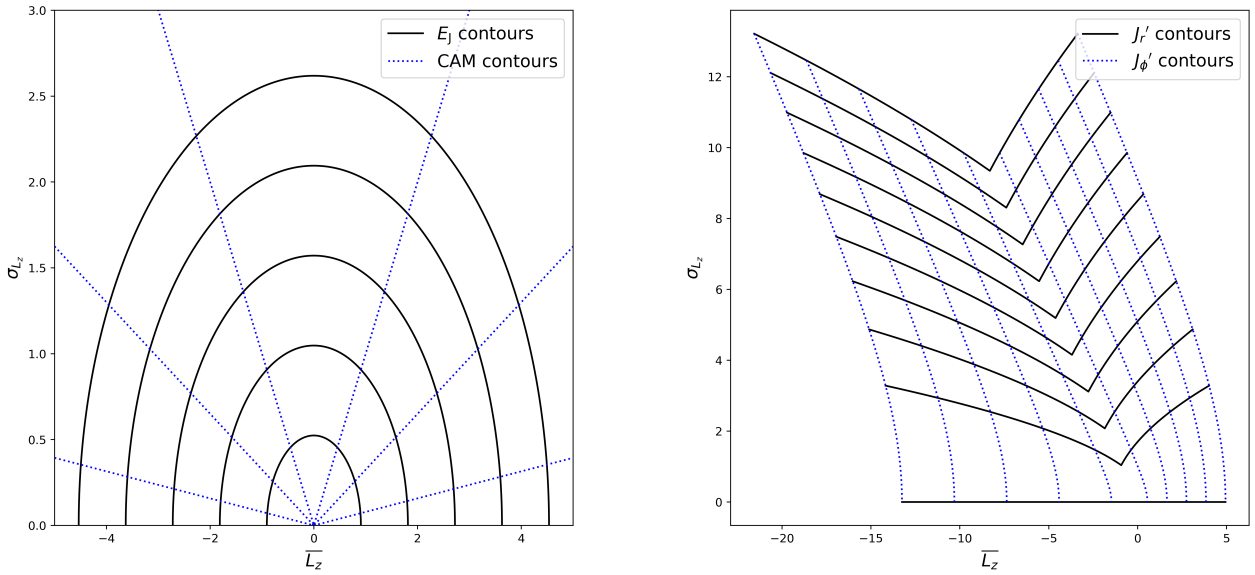

Figure 1. Contours of integrals of motion in the L_z–σ_{L_z} plane for orbits in the Freeman bar model. The left panel displays the E_J contours in black curves and the CAM contours in blue dashed curves. The right panel shows the J_r' contours in black curves and the J_ϕ' contours in blue dashed curves.

We adopt the notation J_r' and J_ϕ' because these quantities reduce exactly to the radial and azimuthal actions, J_r and J_ϕ, in the axisymmetric limit ($\Omega_x = \Omega_y$).

In the axisymmetric case, the radial action is defined by

$$J_r = \frac{1}{\pi}\int_{r_-}^{r_+} v_r dr, \tag{17}$$

where r_- and r_+ are the pericenter and apocenter radii. The azimuthal action J_ϕ corresponds to the angular momentum in the inertial frame and is related to the angular momentum in the corotating frame through

$$J_\phi = L_z + \Omega_b r^2, \tag{18}$$

where r is the cylindrical radius.

In the nonaxisymmetric case, J_r' can be shown to be proportional to the area enclosed by the invariant curves in the r–v_r SoS, obtained by slicing the four-dimensional phase space at ϕ fixed to a constant value,[8] such that

$$J_r' = \frac{1}{2\pi}\iint_D dv_r dr. \tag{19}$$

A similar calculation can be applied to J_ϕ'. We verified the equivalence of Equations (16) and (19) for three randomly selected orbits in the Freeman bar, obtaining agreement at the level of 10^{-5}.

In this new set of action-angle variables, the Hamiltonian can be written as

$$H = \frac{\alpha+\beta}{2}(2J_r' + |J_\phi'|) + \frac{\alpha-\beta}{2}J_\phi'. \tag{20}$$

We can then write CAM as a function of J_r' and J_ϕ',

$$\begin{aligned}\mathrm{CAM} = \frac{\overline{L_z}}{\sigma_{L_z}} &= C_2\frac{J_r' + \frac{\alpha-\beta}{\alpha+\beta}(2J_r' + |J_\phi'|)}{\sqrt{J_r'(J_r' + |J_\phi'|)}} \\ &= C_2\frac{1 + \frac{\alpha-\beta}{\alpha+\beta}(2 + \mathrm{sgn}(l))}{\sqrt{1 + |l|}},\end{aligned} \tag{21}$$

where C_2 is a constant and $l \equiv J_\phi'/J_r'$.

We plot the J_r' and J_ϕ' contours in the $\overline{L_z}$–σ_{L_z} plane, as shown in the right panel of Figure 1. We find that $\overline{L_z}$ is primarily governed by the J_ϕ' contours, which run approximately vertically with a slight slope, whereas σ_{L_z} is mainly characterized by the J_r' contours, which lie roughly along the horizontal direction but twist around the center. Overall, CAM is not strictly proportional to J_ϕ'/J_r' but rather a function of this ratio in the Freeman bar model.

To conclude, we find that in the Freeman bar model, $\overline{L_z}$ primarily reflects the contribution of J_ϕ', which describes the azimuthal motion, whereas σ_{L_z} is mainly determined by J_r', which characterizes the radial motion. Consequently, CAM is determined by the ratio of J_ϕ'/J_r'. In more general bar models, where the actions do not admit analytical expressions, it remains to be tested whether CAM is strictly a function of this ratio. Nevertheless, the Freeman bar model provides valuable insight into the physical nature of CAM.

3. Iso-E_J Orbits and Periodic Orbits in the CAM Framework

To investigate how different orbital families are distributed within the CAM framework, we begin by examining the behavior of iso-E_J orbits, which form regular and continuous sequences in the $\overline{L_z}$–σ_{L_z} plane. We also present the distribution of periodic orbits, which serve as the parent orbits for their associated orbital families. These periodic orbits are fundamental in galactic dynamics, as quasiperiodic

[8] This relation holds only for closed invariant curves. In cases where invariant curves are split segments, the actions must be computed by other means (J. Binney et al. 1985; T.-Y. Xia & J. Shen 2021).

orbits (regular orbits that deviate from periodic ones) are generally trapped and oscillate around their corresponding parent periodic orbits.

In the Freeman bar potential, the iso-E_J orbits in the $\overline{L_z}$–σ_{L_z} plane are shown by the black curves in the left panel of Figure 1, forming the upper portion of an ellipse. The periodic x_1 and x_4 orbits in this model, however, exhibit zero angular momentum dispersion and constant L_z as X_α or X_β equals 0 (see Equation 9), causing their CAM values to diverge. As a result, their properties cannot be meaningfully analyzed within the CAM framework. For this reason, we also consider two additional representative rotating bar potentials: the logarithmic bar and the Ferrers bar in J. A. Sellwood & A. Wilkinson (1993). The logarithmic bar model admits only the x_1 and x_4 orbital families, whereas the Ferrers bar potential also supports the x_2 orbital family. Orbits in these two potentials are integrated for a time span of around 50 dynamical timescales using the python package `Agama`, with a uniform time interval of 0.001 dynamical timescales (E. Vasiliev 2018). We have verified that extending or shortening the integration time by a factor of a few does not affect the main results. The periodic orbits are obtained by launching particles along the x-axis at fixed E_J and identifying those that return to their initial phase-space coordinates.

In this analysis, we focus on low-order resonant periodic orbits located within the corotation radius, as these orbits predominantly contribute to the bar. Higher-order resonant orbits (with resonance order larger than 6) are excluded, as they are often associated with irregular or chaotic behavior and tend to produce complex and less interpretable structures in the parameter space.

In addition to the $\overline{L_z}$–σ_{L_z} plane examined in the original CAM study of QS21, we also explore alternative parameter spaces that directly incorporate the CAM value. Since CAM serves as a proxy for I_2 in addition to E_J, the CAM−E_J plane, resembling the integral-of-motion space, naturally provides a framework for orbital classification. However, because orbits inside and outside the corotation radius overlap in the CAM −E_J plane, an issue discussed in detail in Section 4.2, we instead adopt the CAM−R_{rms} plane, where R_{rms} is defined as the time-averaged rms radius. We find that this parameter space provides a clear separation between orbital families and serves as a critical diagnostic for orbital classification within the CAM framework.

3.1. x_1 and x_4 Orbits

The logarithmic bar potential adopted in this study is identical to that used in QS21, which can be written as

$$\Phi(x, y) = \frac{1}{2} v_0^2 \ln\left(R_c^2 + x^2 + \frac{y^2}{b^2}\right). \quad (22)$$

We take $v_0 = 1$, $R_c = 0.1$, and $b = 0.84$, with a pattern speed of $\Omega_b = 1$. The corotation radius and circular velocity at corotation are $r_{CR} = 0.99$ and $V_{CR} = 0.99$, respectively, owing to the nonzero value of R_c. Radii and velocities are therefore expressed in units of 1.01 r_{CR} and 1.01 V_{CR}. This model only supports x_1 and x_4 orbital families, while x_2 and x_3 orbital families are absent.

Figure 2 shows the distribution of iso-E_J and periodic orbits of the logarithmic bar potential in the $\overline{L_z}$ − σ_{L_z} and CAM −R_{rms} planes, color-coded by E_J. To facilitate comparison between periodic and quasiperiodic orbits, we display the scaled orbital shapes of representative periodic orbits, while quasiperiodic orbits at fixed Jacobi energies are indicated by curves made up of points. We plot the scaled periodic orbits using the following procedure. (i) We divide the parameter space into a 20 × 20 grid. (ii) We randomly select one periodic orbit from each populated grid cell. (iii) We plot the scaled shape of each sampled orbit at its corresponding coordinates in the parameter space.

In the $\overline{L_z}$–σ_{L_z} plane, shown in the left panel of Figure 2, iso-E_J orbits form a continuous sequence from x_4 to x_1 orbits, as discovered by QS21. By comparing them with the periodic orbits, we find that low-E_J orbits are bounded by the x_1 and x_4 periodic orbits, which lie at the endpoints of the iso-E_J contours, as indicated by the labeled branches in the panel. These bounding periodic orbits approximately follow two distinct nonlinear tracks, indicating that they correspond to different values of CAM. At higher E_J, we observe a bifurcation of the x_1 periodic orbit into higher-order resonant families (e.g., the 3:1 resonance), giving rise to additional branches in the $\overline{L_z}$–σ_{L_z} plane.

The right panel of Figure 2 shows the distribution of iso-E_J orbits and periodic orbits in the CAM−R_{rms} plane. We find that R_{rms} increases monotonically with E_J for orbits inside the corotation radius, confirming the advantage of replacing E_J with R_{rms} as the y-axis of the parameter space.

We can clearly identify the morphology evolution for periodic orbits of different orbital families in the CAM−R_{rms} plane. For the x_1 orbits, low-E_J members initially appear as elongated ellipses. As E_J or R_{rms} rises, these orbits transition into lens-shaped configurations, followed by the development of less elongated and more elliptical shapes. At even higher E_J, x_1 orbits display increasingly intricate morphologies, likely associated with higher-order resonant structures. For x_4 orbits, they evolve toward rounder shapes with growing R_{rms}.

Quasiperiodic orbits at fixed E_J also form well-defined curves in the CAM−R_{rms} plane, which represents the unfolded version of the iso-E_J contours in the $\overline{L_z}$–σ_{L_z} plane. Along these curves, CAM increases monotonically when progressing from the x_4 to x_1 orbits, further supporting the validity of CAM as an effective proxy for I_2. This trend is accompanied by a mild variation in R_{rms}, which exhibits a sharp increase near CAM ~ 0 but remains nearly constant otherwise. The variation of R_{rms} along each orbital sequence increases with E_J, while the lowest-E_J orbits show minimal dispersion in R_{rms}.

Similar to the $\overline{L_z}$–σ_{L_z} plane, the x_1 and x_4 periodic orbits mark the boundaries for quasiperiodic orbits and trace two distinct curves. The two boundary lines do not maintain constant |CAM| when R_{rms} increases: the absolute values of CAM for the two boundaries shrink sharply at $R_{rms} \lesssim 0.1$, then vary more gradually at larger R_{rms}.

3.2. x_2 Orbits

While the logarithmic bar potential discussed in Section 3.1 supports only the x_1 and x_4 orbital families, in this section, we adopt the Ferrers bar potential, which accommodates additional families such as x_2 orbits and more accurately represents the orbital structure of barred galaxies.

We adopt the bar potential described by J. A. Sellwood & A. Wilkinson (1993), which comprises an N. M. Ferrers (1877) ellipsoid for the bar component, along with two

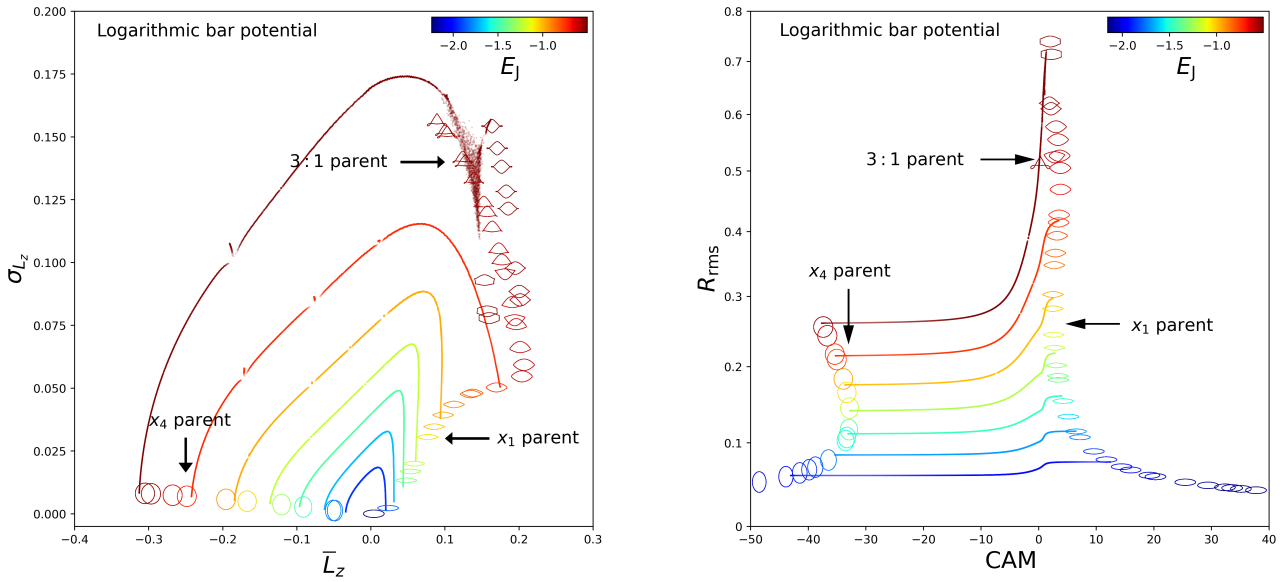

Figure 2. Orbital distributions of the logarithmic bar potential of Equation (22), shown in the L_z–σ_{L_z} plane (left) and the CAM–R_{rms} plane (right), color-coded by E_J. Representative periodic orbits, displayed with their morphological shapes, are superimposed on the distribution, while quasiperiodic orbits appear as colored curves composed of discrete points. Distinct branches corresponding to periodic x_1, x_4, and 3:1 resonant orbits are labeled for reference. The corotation radius is 1.01, and the circular velocity and angular momentum at corotation are 1.01 and 0.98, respectively.

spherically symmetric components, each following a Plummer density profile, representing the bulge and the halo.

The density profile of the bar component is given by

$$\rho_{\rm B} = \begin{cases} \frac{105}{32\pi ac^2} M_{\rm B}(1-\mu^2)^2, & \mu < 1, \\ 0, & \mu \geqslant 1, \end{cases} \tag{23}$$

where

$$\mu^2 = \frac{x^2}{a^2} + \frac{y^2+z^2}{c^2}. \tag{24}$$

We take $M_B = 1.1852$, $a = 1$, and $c = \frac{1}{3}$, which are the same parameters used in J. A. Sellwood & A. Wilkinson (1993).

The Plummer density profile for the spherically symmetric components is

$$\rho_s = \frac{3M_s}{4\pi s^3}\left(1+\frac{r^2}{s^2}\right)^{-\frac{5}{2}}. \tag{25}$$

We adopt $M_s = 0.3$ and $s = 0.05$ for the spheroidal/bulge component and $M_s = 25$ and $s = 1.5$ for the halo component (J. A. Sellwood & A. Wilkinson 1993). The pattern speed is set to be $\Omega_{\rm b} = 2$. The corotation radius and the circular velocity at corotation are $r_{\rm CR} = 1.28$ and $V_{\rm CR} = 2.56$, respectively. All radii and velocities are expressed in units of $0.78\, r_{\rm CR}$ and $0.39\, V_{\rm CR}$.

Following the procedure outlined in Section 3.1, we map representative periodic orbits and iso-E_J orbits in the rotating Ferrers bar potential onto the $\overline{L}_z$–σ_{L_z} and CAM–R_{rms} plane in Figure 3.

For the $\overline{L}_z$–σ_{L_z} plane shown in the left panel of Figure 3, the periodic x_1 and x_4 orbits form two distinct branches that bound the quasiperiodic orbits, similar to the case of the logarithmic bar potential. However, unlike the logarithmic potential, where the quasiperiodic x_1-to-x_4 transition at a fixed E_J traces a smooth and continuous curve, orbits in the Ferrers bar potential exhibit a disruption in this trend. This disruption is caused by chaotic orbits scattered near $\overline{L}_z \sim 0$, particularly at high E_J.

In addition to the x_1 and x_4 orbital families, the x_2 orbits populate regions adjacent to the periodic x_1 branch at low Jacobi energies ($E_J \lesssim -22$), characterized by slightly higher values of $\overline{L}_z$, as labeled in Figure 3. The periodic x_2 orbits form a distinct branch that is topologically connected to the periodic x_1 branch. The closed region bounded by the periodic x_1 and x_2 branches provides a distinct domain for x_2 orbits.

We show the distribution of iso-E_J and periodic orbits in the CAM–R_{rms} plane in the right panel of Figure 3. The contribution of chaotic orbits, which could disrupt the smoothness and continuity of iso-E_J sequences, is negligible, as chaotic orbits possess |CAM| values that are significantly smaller than those of periodic orbits. Consequently, the overall continuity of the orbital sequence from x_4 to x_1 orbits is preserved, leading to smoother and more coherent iso-E_J sequences compared to those seen in the $\overline{L}_z$–σ_{L_z} plane. This property enhances the reliability of orbital classification using the CAM–R_{rms} plane. At certain values of R_{rms}, these trends extend further to reach the x_2 orbits. In these cases, however, the previously observed monotonic increase of R_{rms} with CAM breaks down, and a decreasing trend in R_{rms} appears as the orbital family transitions from x_1 to x_2.

We find that the branch of periodic x_2 orbits is more prominently constructed in the CAM–R_{rms} plane than in the $\overline{L}_z$–σ_{L_z} plane while remaining topologically connected to the branch of periodic x_1 orbits. Together, the periodic x_1 and x_2 branches form a closed region that clearly delineates the x_2 orbital population. This structure provides a robust and visually intuitive framework for distinguishing between x_1 and x_2 orbits.

In addition, we find that some high-order resonance branches can also construct similar closed structures in the CAM–R_{rms} plane. For example, the periodic 3:1 and 4:1 resonance orbital branches, as well as the x_1 orbital branch at high E_J, enclose well-defined regions. These closed regions

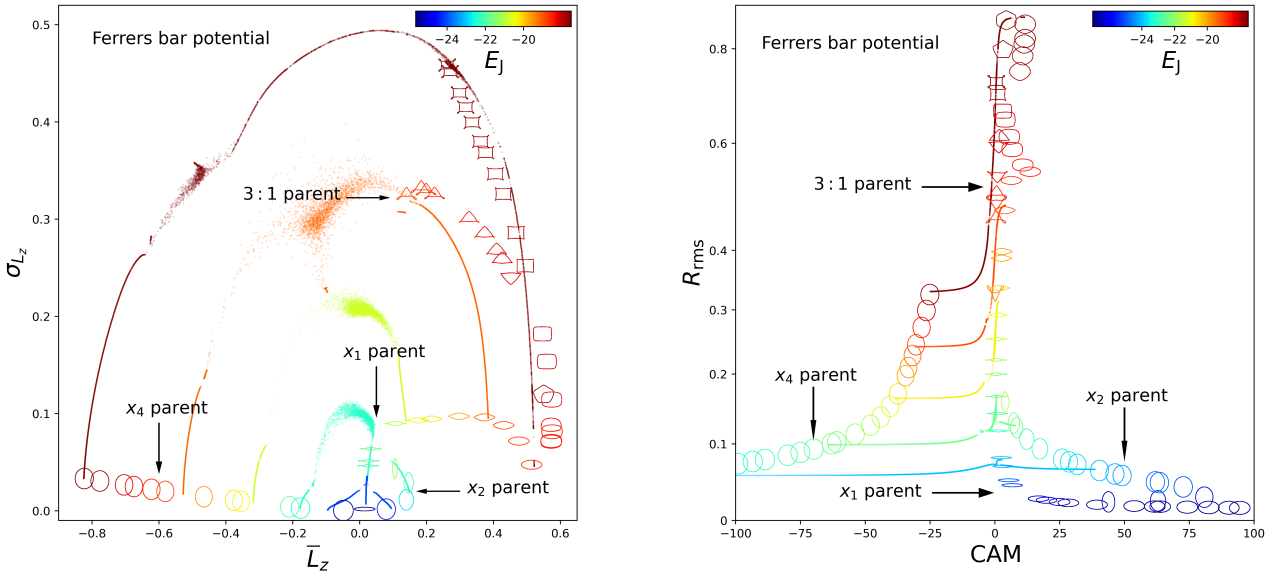

Figure 3. Same as Figure 2 but for the Ferrers bar potential in Section 3.2. Chaotic orbits are shown as scattered points, while quasiperiodic orbits appear as colored curves composed of discrete points. Distinct branches corresponding to periodic x_1, x_2, x_4, and 3:1 resonant orbits are labeled for reference. The corotation radius is 1.28, and the circular velocity and angular momentum at corotation are 2.56 and 3.28, respectively.

may serve as useful indicators for identifying and classifying resonant orbital families.

To conclude, our analysis demonstrates that periodic orbits trace well-defined branches in the CAM–R_{rms} plane, effectively separating the parameter space into distinct regions occupied by quasiperiodic orbits of specific orbital families. This clear structure highlights the effectiveness of the CAM–R_{rms} plane as a robust framework for orbital classification.

4. Test-particle Orbits in the CAM Framework

To more closely mimic real orbits in barred galaxies, we use orbits drawn from simple 2D test-particle simulations in three static bar potentials, including the Freeman bar, the logarithmic bar, and the Ferrers bar potentials. These orbits span a broader range of E_J and include the main orbital families associated with each bar model, thereby providing an overall view of the orbital distribution.

The simulation is set up by generating test particles with simple initial conditions as follows. (i) The initial radius R is drawn from an exponential distribution with scale length $r_d = 2.2$, such that the probability density is proportional to $\exp(-R/r_d)$. We have verified that the specific choice of radial profile does not affect the final results. The initial azimuthal angle ϕ is uniformly distributed between 0 and 2π. (ii) The initial velocities in the radial and azimuthal directions are sampled from different Gaussian distributions. The mean radial velocity is set to 0, while the mean azimuthal velocity is equal to the rotation velocity of the corresponding potential model. The isotropic velocity dispersion is set to 0.4 for the Freeman bar, 1 for the Ferrers bar potentials, and 0.5 for the logarithmic bar potential. These values are approximately half of the rotation velocity at corotation and are chosen to ensure a wide range of orbital behaviors, with the exception of the Freeman bar, which does not possess a corotation radius. We further verify that varying the velocity dispersion by up to 50% primarily affects the density of the orbital distribution, without altering its qualitative structure. We integrate the orbits by using the python package `Agama` (E. Vasiliev 2018).

In addition to the CAM–R_{rms} plane, we also examine the distribution of test-particle orbits in the CAM–E_J plane, which resembles the integral-of-motion space. We verify that the CAM–R_{rms} plane provides a more effective tool for orbital classification.

4.1. Freeman Bar Potential

The Freeman bar is indeed overly simplistic and idealized: it lacks a corotation radius and exhibits a rotation velocity that varies linearly with radius, which significantly deviates from the behavior of real barred galaxy potentials. Nevertheless, it can still serve as a useful local model for approximating bar orbits.

We plot the distribution of test-particle orbits for the Freeman bar potential in the CAM–E_J and CAM–R_{rms} planes, as shown in Figure 4. The panels are generated following the procedure described in Section 3.1.

We find a well-ordered transition from x_4 orbits to x_1 orbits in both the CAM–E_J and CAM–R_{rms} planes, where x_4 orbits occupy the left side of the diagrams, characterized by negative CAM, while x_1 orbits lie on the right with positive CAM. The parallel trends in these two planes arise from a smooth correlation between E_J and R_{rms}. We label the approximate regions corresponding to the x_1 and x_4 orbital families, as there is no well-defined boundary between these two orbital families. In the left panel, the trend of orbits with similar spatial extents arises because E_J depends on angular momentum. In the right panel, we overplot iso-E_J sequences in this parameter space, shown as the colored dashed curves in the right panel of Figure 4, which are broadly consistent with the trends seen in the logarithmic bar potential (right panel of Figure 2).

The noticeable shrinkage of the orbital distribution boundaries as E_J or R_{rms} increases is caused by the initial conditions in our setup, which reduce the probability of generating orbits

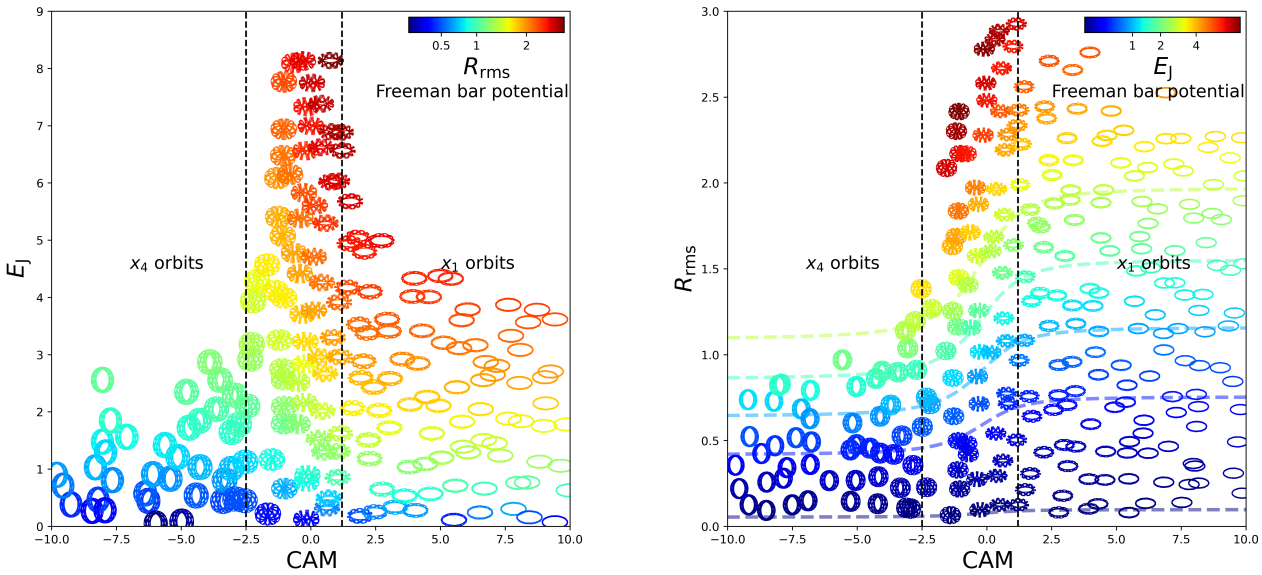

Figure 4. Orbital distribution in the Freeman bar model, shown in the CAM–$E_{\rm J}$ plane (left) and the CAM–$R_{\rm rms}$ plane (right). Scaled orbits are plotted at their corresponding locations in both parameter spaces. The left panel is color-coded by $R_{\rm rms}$, while the right panel is color-coded by $E_{\rm J}$. The approximate regions of the x_1, x_2, and x_4 orbital families are outlined by black dashed lines, and the colored dashed curves in the right panel trace the general trends of orbits at fixed $E_{\rm J}$.

close to periodic orbits, which tend to exhibit large |CAM|. Although this behavior is common to our test-particle simulations for all rotating bar potentials, the Freeman bar potential is a special case: its periodic x_1 and x_4 orbits have formally infinite |CAM| and therefore do not provide meaningful boundaries for the quasiperiodic orbits.

Overall, both the CAM–$E_{\rm J}$ and CAM–$R_{\rm rms}$ planes provide effective tools for orbit classification in the Freeman bar potential. Given the highly idealized nature of the Freeman bar, we therefore extend our analysis to more widely used models, the logarithmic and Ferrers bar potentials, to assess the applicability of these parameter spaces in more realistic settings.

4.2. Logarithmic Bar Potential

Similar to the case of the Freeman bar, we plot the orbital distribution of the logarithmic bar potential given by Equation 22, as well as the scaled shapes of representative orbits, in the CAM–$E_{\rm J}$ and CAM–$R_{\rm rms}$ planes in Figure 5. We find that the x_1 and x_4 orbital distributions in this potential closely resemble those in the Freeman bar potential, where x_1 orbits occupy the lower right region with CAM > 0 and x_4 orbits are found in the lower left region with CAM < 0. This also agrees with the iso-$E_{\rm J}$ trend found by Figure 2.

However, we notice that the region associated with the x_4 orbital family in the CAM–$E_{\rm J}$ plane is heavily populated by orbits located beyond the corotation radius. When color-coding orbits by $R_{\rm rms}$, we find that the continuous sequence from x_4 to x_1 orbital families becomes becomes disrupted by the presence of large-radius orbits. Orbits beyond the corotation radius, which rotate more slowly than the bar pattern speed and exhibit low $E_{\rm J}$ due to their large radius, introduce contamination into the x_4-to-x_1 sequence. These resulting degeneracies between orbits within and beyond the corotation radius fundamentally limit the utility of the CAM–$E_{\rm J}$ plane for reliable orbital classification. In contrast, such contamination does not occur in the Freeman bar model due to the absence of a defined corotation radius, as shown in the left panel of Figure 4. Nevertheless, the CAM–$E_{\rm J}$ plane remains a useful diagnostic for bar orbits once orbits outside the corotation radius are removed, as demonstrated in the Appendix.

In contrast, the CAM–$R_{\rm rms}$ plane effectively removes the degeneracies caused by the overlap of orbits inside and outside the corotation radius, yielding a clean distribution of orbital families. To highlight the progression of orbits at fixed $E_{\rm J}$, we fit cubic splines to the iso-$E_{\rm J}$ sequences in the right panel of Figure 2, since iso-$E_{\rm J}$ orbits do not strictly form curves in logarithmic bar potentials, and plot the resulting trends as colored dashed curves in the right panel of Figure 5. In addition, we note that the |CAM| values along the envelopes of the orbit population in the CAM–$R_{\rm rms}$ plane exhibit more pronounced variations than those in the right panel of Figure 2, primarily because the two plots employ different ranges on the CAM axis.

Within the corotation radius, the morphological evolution of quasiperiodic x_1 and x_4 orbits with increasing $R_{\rm rms}$ or $E_{\rm J}$ closely follows that of the parent periodic orbits in Figure 2. When $R_{\rm rms}$ reaches the corotation radius, the x_4 and x_1 orbits become trapped near the corotation region. In this regime, the x_4 orbits transition into short-period orbits, while the x_1 orbits evolve into horseshoe orbits, commonly referred to as long-period orbits (J. A. Sellwood & A. Wilkinson 1993).

Orbits beyond the corotation radius also exhibit well-ordered distributions in our analysis. These orbits consistently display negative CAM, as their rotation lags behind the bar pattern speed. Due to the averaging of the nonaxisymmetric forces, they generally maintain nearly circular shapes and form narrow, rosette-like annuli with large |CAM| values. The outermost orbits, which have large $R_{\rm rms}$, correspond to the lowest values of $E_{\rm J}$ and are therefore more tightly bound. This behavior follows directly from the definition of the Jacobi energy,

$$E_{\rm J} = \frac{1}{2}|\dot{\boldsymbol{r}}|^2 + \Phi(\boldsymbol{r}) - \frac{1}{2}\Omega_{\rm b}^2 r^2, \tag{26}$$

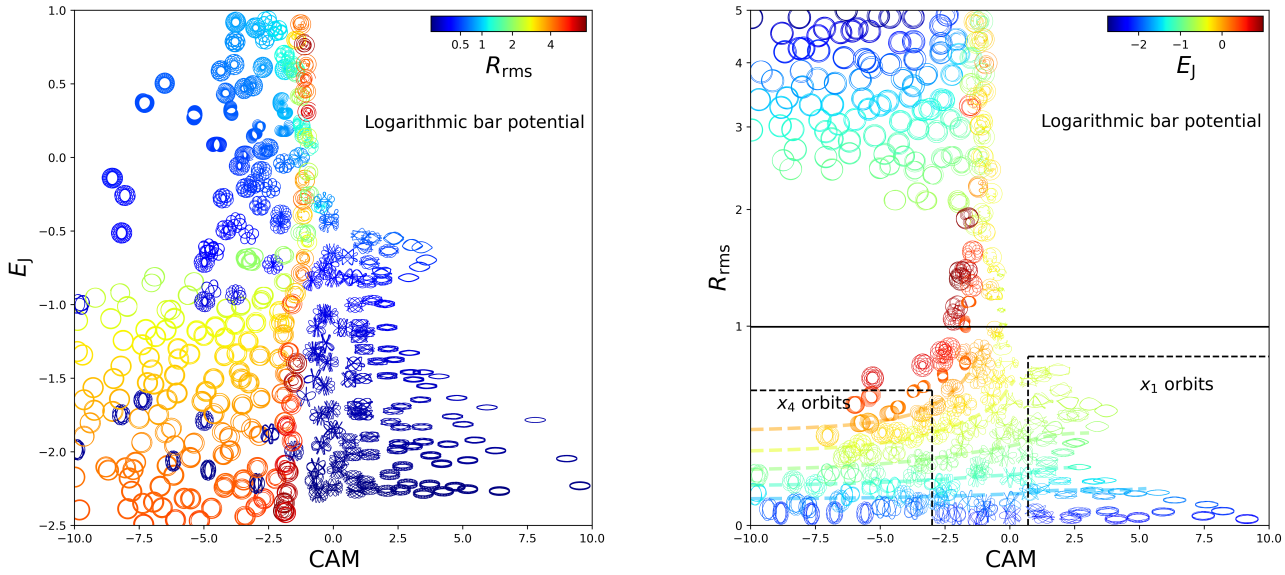

Figure 5. Same as Figure 4 but for the logarithmic bar potential. In the right panel, the approximate regions of the x_1 and x_4 orbital families are outlined by black dashed lines, and the solid black horizontal line marks the corotation radius. The colored dashed curves trace the general trends of orbits at fixed $E_{\rm J}$.

where $\boldsymbol{r}$ and $\dot{\boldsymbol{r}}$ are defined in the corotation frame. For nearly circular orbits outside the corotation radius, the centrifugal term decreases more rapidly with increasing $R_{\rm rms}$ than the kinetic and gravitational potential terms, leading to lower $E_{\rm J}$ for larger $R_{\rm rms}$.

In addition, we identify high-$E_{\rm J}$ orbits with CAM ~ 0 in this region, primarily corresponding to unstable trajectories that would eventually escape the system under longer integration times.

4.3. Ferrers Bar Potential

To investigate the x_2 orbits, we map representative scaled orbits in the rotating Ferrers bar potential, of which the density profile is given by Equations (23) and (25), onto the CAM–$E_{\rm J}$ and CAM–$R_{\rm rms}$ planes, as shown in Figure 6.

Similar to the logarithmic bar potential, the x_4 orbits in the CAM–$E_{\rm J}$ plane are contaminated by orbits beyond the corotation radius, whereas a clean transition between the x_4 and x_1 orbital families within the corotation radius is revealed in the CAM–$R_{\rm rms}$ plane. As in the logarithmic bar case, we mark the fixed-$E_{\rm J}$ trends in Figure 6 with colored dashed lines, obtained by applying cubic-spline fits to the iso-$E_{\rm J}$ sequences in the right panel of Figure 3, after excluding chaotic orbits.

In particular, we find that the x_2 orbits emerge at low $R_{\rm rms}$ and high CAM, occupying a distinct region in the CAM–$R_{\rm rms}$ plane. These orbits are situated between the lens-shaped and boxy x_1 orbits at $0.05 \lesssim R_{\rm rms} \lesssim 0.25$ and exhibit larger CAM values than the x_1 orbits of comparable size, as depicted by the labeled regions for the x_2 orbital family in the right panel of Figure 6. This location is consistent with the closed region bounded by the periodic x_1 and x_2 orbits in Figure 3. As a result, x_2 orbits show little overlap with the x_1 family in the CAM–$R_{\rm rms}$ plane, making this parameter space particularly effective for distinguishing between these two orbital families.

To conclude, the CAM–$R_{\rm rms}$ plane proves to be an effective and robust tool for orbital classification. It can be readily applied to snapshots of realistic N-body simulations, enabling the identification of major orbital families without requiring fixed-$E_{\rm J}$ sampling.

5. Discussion

5.1. Strengths and Weaknesses

Compared with conventional orbital classification tools, the CAM diagnostic exhibits several key advantages. First, as a numerical proxy for the second integral of motion, CAM is intrinsically independent of the Jacobi energy. It retains much of the dynamical information typically extracted from SoS but without requiring orbits to be analyzed at fixed $E_{\rm J}$. This makes CAM particularly well suited for studying test particles in barred galaxy models, where orbits span a continuous range of Jacobi energies, in contrast to the SoS, which is restricted to discrete $E_{\rm J}$ slices. Second, CAM constrains orbital structure through phase-space averaging rather than direct projection, enabling a natural extension to 3D orbits through the incorporation of an additional proxy for the third integral of motion. Finally, because CAM directly reflects intrinsic orbital properties as an integral-like quantity, it exhibits reduced degeneracy compared with frequency analysis, with distinct orbital families occupying nonoverlapping regions.

Despite these advantages, we list its potential limitations below.

The primary limitation of our method lies in the lack of quantitative criteria for distinguishing orbital families across different bar potentials. Because the locations of periodic-orbit branches can vary systematically among models, the mapping between orbital families and their corresponding regions in the CAM–$R_{\rm rms}$ plane is not universally defined. This issue becomes more pronounced for higher-order resonant orbits, whose domains in the CAM–$R_{\rm rms}$ plane may connect with multiple families. As a result, additional computational effort is required to solve for the relevant periodic orbits in each potential.

Another limitation arises from the reduced effectiveness of the method in identifying chaotic orbits, particularly at higher $E_{\rm J}$, where such orbits become more prevalent.

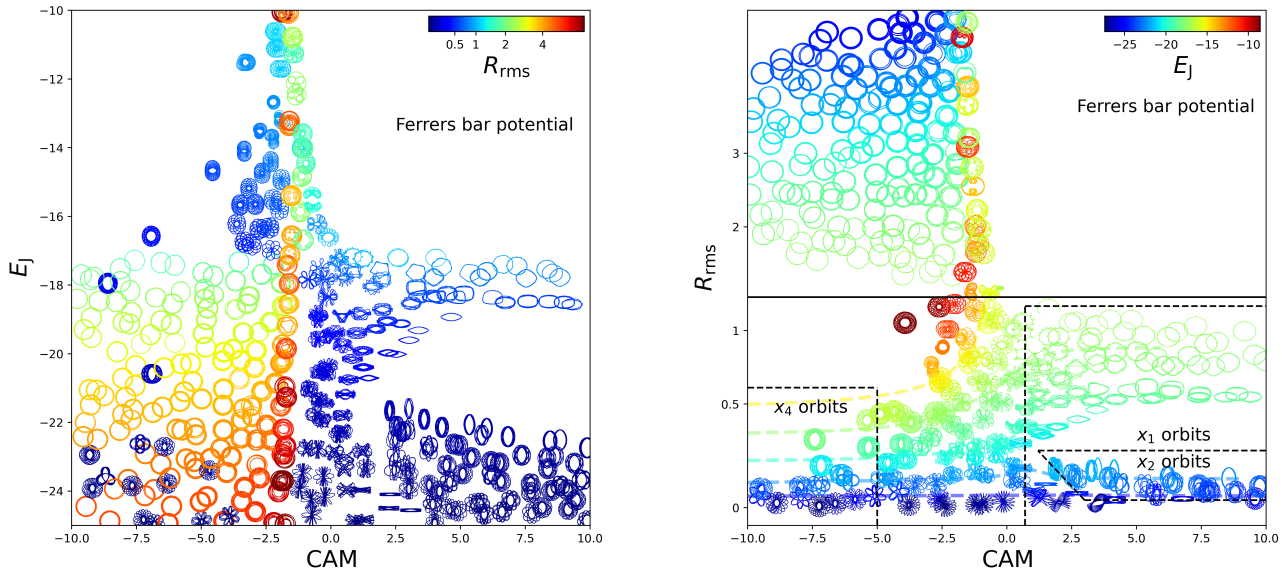

Figure 6. Same as Figure 2 but for the Ferrers bar potential. The approximate regions of the x_1, x_2, and x_4 orbital families are outlined by black dashed lines.

This shortcoming stems from the fact that chaotic orbits do not preserve a well-defined second or third integral of motion, which undermines the applicability of CAM as a numerical proxy. Although chaotic orbits can be approximately located in the $\overline{L_z}$–σ_{L_z} plane, their boundaries, unlike those of quasiperiodic orbits, cannot be anchored to periodic-orbit curves and therefore remain difficult to define rigorously. Further work is needed to develop quantitative criteria for identifying and isolating chaotic components within this framework.

5.2. Application to 3D Orbits

Extending this framework to 3D orbital classification requires identifying an additional proxy that effectively captures the third integral of motion, I_3. Following the approximation schemes employed in the 2D case, a promising candidate we identified is the ratio of the time-averaged vertical action ($\overline{J_z}$) to the temporal dispersion of the angular momentum (σ_{L_z}). The vertical action is defined as $J_z = \int_{z_{\rm min}}^{z_{\rm max}} v_z dz$, where $z_{\rm max}$ and $z_{\rm min}$ denote the turning points of a single vertical oscillation. We find that 3D orbits at fixed $E_{\rm J}$ trace a similar sequence in the $\overline{L_z}$–σ_{L_z} plane to the 2D case, when they are grouped into bins of $\overline{J_z}/\sigma_{L_z}$, suggesting that this ratio may serve as a possible proxy for I_3. Therefore, the CAM–$R_{\rm rms}$ plane for 3D orbits can be constructed within each $\overline{J_z}/\sigma_{L_z}$ bin, potentially enabling effective 3D orbital classification. A detailed investigation and validation of these approaches will be presented in a forthcoming study.

5.3. Application to N-body Simulations

Here we briefly clarify how the method can be applied to particles in a realistic N-body simulation snapshot. For a given snapshot, one can extract the phase-space coordinates ($\boldsymbol{x}_n$, $\boldsymbol{v}_n$) for particles, together with the frozen gravitational potential associated with the snapshot. To classify the orbital families represented by these particles, the following steps can be adopted.

(i) Integrate snapshot particles in the corresponding frozen potential. The quantities $\overline{L_z}$, σ_{L_z}, and $R_{\rm rms}$ can be computed by time-averaging along the resulting orbits, and CAM is defined as the ratio $\overline{L_z}/\sigma_{L_z}$.

(ii) Construct the CAM–$R_{\rm rms}$ plane. The corotation radius that separates bar-supporting orbits from those outside the corotation radius can be identified from the location in $R_{\rm rms}$ where a sharp decrease in the number of orbits at positive CAM occurs (as illustrated by the black solid line in the right panel of Figure 5). Approximate clusters associated with different orbital families may then be identified by overplotting representative scaled orbits on this diagram, as shown in Figures 5 and 6.

(iii) To resolve finer orbital structure, the periodic orbits that define the boundaries of different families must be computed in the frozen potential. Chaotic orbits can be identified in the $\overline{L_z}$–σ_{L_z} plane as regions of scattered points that deviate from the well-defined curves traced by quasiperiodic curves obtained from the iso-$E_{\rm J}$ sequence, as shown in the left panel of Figure 3.

6. Conclusion

In this paper, we propose a new method for 2D orbital classification by using a proxy of the second integral of motion, CAM, defined as the ratio of the time-averaged angular momentum to its temporal dispersion in the corotating frame.

We begin by analytically examining the physical interpretation of CAM within the Freeman bar model. Our analysis shows that $\overline{L_z}$ is dominated by the contribution from J_ϕ', which describes the azimuthal motion, whereas σ_{L_z} is largely governed by J_r', representing the radial motion. Consequently, CAM depends on the ratio J_ϕ'/J_r' in the Freeman bar, offering valuable insight into its physical nature.

We construct a new parameter space defined by CAM and the rms radius ($R_{\rm rms}$). We do not adopt the conventional integral-of-motion space defined by CAM and $E_{\rm J}$, as it exhibits degeneracies arising from orbits outside the corotation radius.

We test our method in three rotating barred potentials: the Freeman bar, the logarithmic bar, and the Ferrers bar. We find that periodic orbits trace distinct branches in the CAM–$R_{\rm rms}$ plane, effectively partitioning it into regions occupied by their corresponding orbital families. Notably, some of these branches form closed areas that allow clear identification of specific families, such as the x_2 orbits. We further extend our analysis to test-particle orbits spanning a wide range of $E_{\rm J}$ and confirm that different orbital families exhibit a well-ordered distribution in this plane with no spatial overlap.

To conclude, we demonstrate that CAM versus the rms radius plane provides an effective framework for orbital classification in rotating bar potentials. As CAM is fundamentally linked to the intrinsic properties of orbits, it is particularly well suited for application in N-body simulations and can be naturally extended to 3D cases. Although CAM may display ambiguous behavior for higher-order resonant or chaotic orbits, it nonetheless represents a valuable complement to conventional orbital classification methods, such as the SoS and frequency analysis method, owing to its simplicity and computational efficiency when applied to individual orbits.

Acknowledgments

We thank James Binney for useful comments. The research presented here: is partially supported by the National Natural Science Foundation of China under grant Nos. 12533004, 12025302, 11773052; by China Manned Space Program with grant no. CMS-CSST-2025-A11; by the "111" Project of the Ministry of Education of China under grant No. B20019; and by Office of Science and Technology, Shanghai Municipal Government with grant Nos. 24DX1400100 and ZJ2023-ZD-001. This work has made use of the Gravity Supercomputer at the Department of Astronomy, Shanghai Jiao Tong University.

Appendix
CAM–$E_{\rm J}$ Space for Orbits Inside the Corotation Radius

In this section, we examine how orbits inside the corotation radius of the logarithmic and Ferrers bar potentials are distributed in the CAM–$E_{\rm J}$ plane, as shown in Figure 7. The CAM–$E_{\rm J}$ plane can be viewed as an alternative to the CAM–$R_{\rm rms}$ plane once all orbits outside corotation are removed. In both representations, bar-supporting orbits exhibit similar morphological distributions.

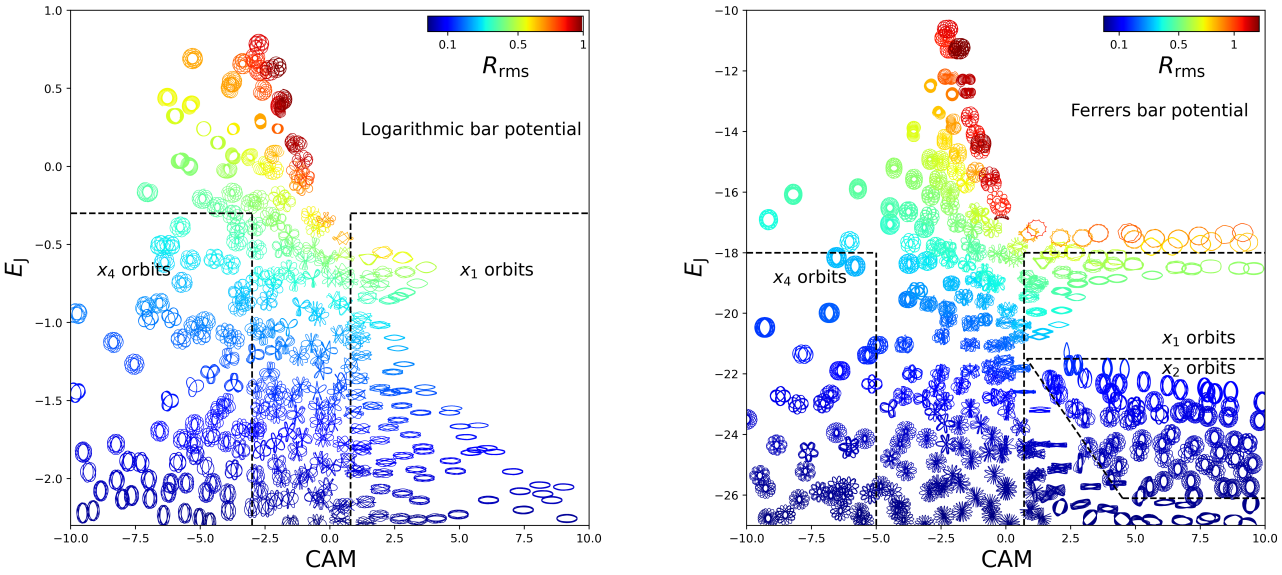

Figure 7. Distribution of orbits inside the corotation radius in the CAM–$E_{\rm J}$ plane for the logarithmic bar potential (left) and the Ferrers bar potential (right), color-coded by $R_{\rm rms}$. Scaled orbits are plotted at their corresponding locations in both panels. The approximate regions of the x_1, x_2, and x_4 orbital families are outlined by black dashed lines.

ORCID iDs

Tian-Ye Xia https://orcid.org/0000-0003-1309-3050
Juntai Shen https://orcid.org/0000-0001-5604-1643
John Magorrian https://orcid.org/0000-0001-6127-6957
Yu-jing Qin https://orcid.org/0000-0003-3658-6026

References

Binney, J., Gerhard, O. E., & Hut, P. 1985, MNRAS, 215, 59
Binney, J., Gerhard, O. E., Stark, A. A., Bally, J., & Uchida, K. I. 1991, MNRAS, 252, 210
Binney, J., & Spergel, D. 1982, ApJ, 252, 308
Binney, J., & Tremaine, S. 2008, Galactic Dynamics: Second Edition (2; Princeton Univ. Press)
Carpintero, D. D., & Aguilar, L. A. 1998, MNRAS, 298, 1
Contopoulos, G., & Grosbol, P. 1989, A&ARv, 1, 261
Ferrers, N. M. 1877, QJPAM, 14, 1
Freeman, K. C. 1966, MNRAS, 133, 47
Freeman, K. C., & Mestel, L. 1966, MNRAS, 134, 15
Laskar, J. 1993, CeMDA, 56, 191
Pfenniger, D., & Friedli, D. 1991, A&A, 252, 75
Poincaré, H. 1892, Les Methodes Nouvelles de la Mchanique Celeste, Vol. II (Gauthier-Villars)
Qin, Y.-J., & Shen, J. 2021, ApJL, 913, L22
Sellwood, J. A., & Wilkinson, A. 1993, RPPh, 56, 173
Shen, J., Rich, R. M., Kormendy, J., et al. 2010, ApJL, 720, L72
Shen, J., & Sellwood, J. A. 2004, ApJ, 604, 614
Shen, J., & Zheng, X.-W. 2020, RAA, 20, 159
Skokos, C., Patsis, P. A., & Athanassoula, E. 2002a, MNRAS, 333, 847
Skokos, C., Patsis, P. A., & Athanassoula, E. 2002b, MNRAS, 333, 861
Sparke, L. S., & Sellwood, J. A. 1987, MNRAS, 225, 653
Valluri, M., Debattista, V. P., Quinn, T., & Moore, B. 2010, MNRAS, 403, 525
Valluri, M., Shen, J., Abbott, C., & Debattista, V. P. 2016, ApJ, 818, 141
van Albada, G. D. 1983, IAUS, 100, 227
Vasiliev, E. 2018, MNRAS, 482, 1525
Voglis, N., Harsoula, M., & Contopoulos, G. 2007, MNRAS, 381, 757
Xia, T.-Y., & Shen, J. 2021, ApJ, 921, 162